

# Study of the Properties of Iron and Vanadium Nitride Coatings by CCPD on 1080 Steel

Marcos Cristino de S. Brito<sup>a</sup>, Brenda Jakellinny S. Nôleto<sup>a</sup>, Lucas Pereira da Silva<sup>a</sup>,  
Renan Matos Monção<sup>a</sup>, Juliermes Carvalho Pereira<sup>b</sup>, Maria Gerlania O. Queiroz<sup>c\*</sup> ,  
Edivan Silva de Oliveira<sup>c</sup>, José César A. de Queiroz<sup>c</sup>,  
Thercio Henrique C. Costa<sup>c</sup>, Rômulo Ribeiro M. Sousa<sup>c</sup> 

<sup>a</sup>Universidade Federal do Piauí, Programa de Pós-Graduação em Engenharia e Ciência dos Materiais, 64049-550, Teresina, PI, Brasil.

<sup>b</sup>Universidade Estadual do Maranhão, Departamento de Matemática e Física, 65604-380, Caxias, MA, Brasil.

<sup>c</sup>Universidade Federal do Rio Grande do Norte, Programa de Pós-Graduação em Engenharia Mecânica, 59072-970, Natal, RN, Brasil.

Received: September 16, 2023; Revised: February 22, 2024; Accepted: March 16, 2024

In this study, nanostructured coatings of VN<sub>2</sub>/Fe<sub>3</sub>N/Fe<sub>4</sub>N are synthesized by Plasma Deposition (CCPD) using a vanadium cathodic cage and subject to cathodic and floating potential treatments. Microstructural and mechanical properties of coated SAE 1080 steel samples are investigated using X-ray Diffraction (XRD), Scanning Electron Microscopy (SEM), Vickers microhardness (HV), and surface roughness analysis. The coating produced under cathodic potential treatment exhibited a nitride-based microstructure (VN<sub>2</sub>, Fe<sub>3</sub>N, Fe<sub>4</sub>N), with surface morphology consisting of clusters of granular structures with varied particle sizes. The coating produced under floating potential predominantly exhibited the iron nitride phase (Fe<sub>3</sub>N) with a morphology composed of uniformly sized grains. Microhardness testing showed that both layers exhibited more excellent plastic deformation resistance than the substrate. Roughness measurements confirmed a more organized microstructure profile for the sample treated under floating potential. This study demonstrates that the CCPD-produced cathodic potential coating can be utilized in tribological applications.

**Keywords:** CCPD deposition, cathodic cage, vanadium nitride, plasma.

## 1. Introduction

Plasma nitriding significantly improves the mechanical and tribological properties of materials exposed to ionized gas mixtures, typically rich in nitrogen<sup>1</sup>. By forming a nitride-rich layer on the material's surface, distinct characteristics emerge, such as corrosion resistance. This makes steel particularly suitable for applications requiring high mechanical performance<sup>2,3</sup>.

Vanadium nitride (VN) has garnered research attention due to its versatile applications, including coating for cutting tools<sup>4</sup>, components in internal combustion engines<sup>5</sup>, heat sinks<sup>6</sup>, and as an additive in alloy manufacturing<sup>7</sup>. Furthermore, vanadium nitride coatings exhibit protective capabilities for metallic alloys<sup>8</sup>, electronic shielding<sup>9</sup>, and systems operating under extreme temperature and pressure conditions<sup>10,11</sup>.

The literature reports the use of various plasma processing techniques for the deposition of vanadium nitride coatings<sup>12-15</sup>. These techniques come with limitations, such as environmental issues<sup>16</sup>, low deposition efficiency<sup>17</sup>, and unsuitability for large-scale processing<sup>18</sup>, due to complex equipment and high costs<sup>19</sup>. In conventional plasma nitriding, samples are treated at a cathodic potential, directly bombarded by high-energy plasma ions, allowing nitrogen to react with the metallic

material's surface, forming a hardened layer of nitrides<sup>20</sup>. During this process, ion-surface interactions can sometimes lead to overheating<sup>21</sup>, edge effect, and hollow cathode effect due to the high cathodic potential on the sample's surface<sup>22-24</sup>. To minimize the limitations of conventional nitriding, more than two decades of research have led materials scientists to develop a new technology initially referred to as active screen plasma, which is currently reported as Cathodic Cage Plasma Deposition (CCPD)<sup>22,23,25-28</sup>. In this process, samples are maintained at a floating potential, and a screen (cathodic cage) is added to enclose the samples and act as the cathode<sup>25</sup>. Film formation occurs due to the material being sputtered from the cell. Simultaneously, a hard nitride layer forms beneath the deposited film due to the diffusion of implanted nitrogen atoms into the sample. This layer can act as a barrier to the diffusion of unwanted interstitial elements (oxygen and its oxides)<sup>20</sup>. Due to the absence of direct ion bombardment on the sample surface, it is possible to reduce or eliminate overheating and edge effects. Factors such as the chemical composition of the cage material, applied potential, gas mixture, gas pressure, time, and temperature can result in films with an excellent mechanical and tribological response<sup>25</sup>.

\*e-mail: mariagerlania@hotmail.com

The literature reports the use of different alloys (silver<sup>29</sup>, copper<sup>30</sup>, titanium<sup>31</sup>, nickel<sup>32</sup>, chromium<sup>33</sup>, nickel/chromium<sup>34</sup>) in the composition of the cage for the treatment of metallic samples<sup>26</sup>. Macedo et al.<sup>35</sup>, increased samples' hardness and wear resistance with niobium cathodic cage plasma treatment. Silva et al.<sup>26</sup>, demonstrated that CCPD on stainless steel exhibited good performance in terms of corrosion resistance at low temperatures (350°C). Medeiros et al.<sup>36</sup>, performed CCPD treatment on AISI 6160 samples using a Hastelloy C-276 alloy cage. The authors showed that the steel exhibited higher surface hardness and wear resistance compared to samples subjected only to conventional nitriding.

Like all transition metal nitrides (Group VB), VN possesses relevant mechanical properties<sup>8</sup>, a high melting point<sup>18</sup>, high electrical and thermal conductivity<sup>37</sup>, good catalytic activity<sup>38</sup>, and considerable resistance to oxidative processes<sup>9</sup>. However, a report suggests that the tribomechanical properties of VN are influenced by surface roughness and texture, which consequently reflect the degree of microstructural network organization<sup>39</sup>. Additionally, according to the author, the synthesis of VN assisted by various plasma treatments and the analysis of its mechanical response to wear need to be explored in greater depth.

Hence, comprehending the microstructure formation dynamics of this film in conjunction with the deposition parameters adopted during the treatment is essential for producing high-quality VN coatings. Given the scarcity of studies on this nitride, there is a need to investigate the relationship between the mechanical and physical properties of VN and the process parameters. In this way, CCPD emerges as a promising technique capable of synthesizing these nitrides with high quality for characterization.

In this context, this study aims to investigate the microstructural and mechanical aspects of films deposited by CCPD with a vanadium cage at different polarization potentials (floating and cathodic) on SAE 1080 steel samples.

## 2. Materials and Methods

Samples of SAE 1080 steel used in this study, with a chemical composition (wt%) of 0.75 - 0.88% C, 0.60 - 0.90% Mn, max 0.030% P, max 0.050% S, and Fe balance, were commercially acquired. The samples were cut under cooling in a cubic geometry (20 x 20 x 5 mm<sup>3</sup>). After missing, the samples underwent metallographic preparation according to ASTM E3-11 (2017) standard. The plasma nitriding reactor used to treat the samples is described in references<sup>25,40-42</sup>. In the first treatment, a model was positioned on an insulating material disk (Al<sub>2</sub>O<sub>3</sub>) to maintain it at a floating potential. In contrast, in the second treatment, the sample was placed directly on the sample holder, subjecting it to a cathodic potential. In both treatments, the samples were kept inside a cathodic cage made of vanadium with dimensions of 35 mm in height, 70 mm in diameter, 3 mm in thickness, and uniformly spaced holes with a diameter of 8 mm.

In both treatments, the samples underwent a pre-sputtering process for 1 hour at 623.15 K in an argon-hydrogen mixture (45 cm<sup>3</sup>/min - 50% Ar + 50% H<sub>2</sub>) to remove surface contaminants. For the treatment at a floating potential, despite the lower quantity of ions bombarding the sample surface compared to the cathodic potential treatment, these ions still

have sufficient minimum energy to clean the surface<sup>43</sup>. The floating and cathodic potential treatments were conducted at 673.15 K for 3 hours using a nitrogen-hydrogen mixture (75 cm<sup>3</sup>/min of N<sub>2</sub> - 25 cm<sup>3</sup>/min of H<sub>2</sub>).

The samples were characterized by X-ray diffraction (Shimadzu DRX-6000) using Cu-K $\alpha$  radiation ( $\lambda = 1.55418 \text{ \AA}$ ). The copper tube was operated at a voltage of 45 kV, a current of 40 mA, and a  $2\theta$  scanning range from 30° to 90°. Vickers microhardness testing (INSIZE model ISH-TDV 1000 A-B) was performed with a 25 gf load, resulting in an average value from five measurements. Topographical and cross-sectional analysis was conducted via scanning electron microscopy (SEM) using the FEI COMPANY QUANTA FEG 250 model. Roughness testing was carried out using a profilometer (MITUTOYO model SJ-210), with four measurements on each sample, an evaluation length of 12.5 mm, and a sampling length of 2.5 mm.

## 3. Results and Discussion

The phase structures of the substrate (base material) and the samples treated with a vanadium cage at different potentials (cathodic and floating) are shown in the diffraction pattern in Figure 1. For the base material, diffraction peaks related to the  $\alpha$ -Fe phase - ICSD 064998, typical of the ferrite structure present in SAE 1080 steel, are observed. The cathodic potential treatment resulted in the appearance of phases of vanadium nitride-II (VN<sub>2</sub>) - ICSD 144473, iron nitride-III (Fe<sub>3</sub>N) - ICSD 080930, and iron nitride-IV (Fe<sub>4</sub>N) - ICSD 060195. As in other cases<sup>20,25,44</sup>, the formation of these primary iron nitrides was expected. The emergence of the VN<sub>2</sub> phase is related to the CCPD deposition process in which the cage material undergoes sputtering. Vanadium atoms stripped from the cage react with the nitrogen-rich atmosphere, and the resulting interaction product (gas + cage) is deposited on the sample surface<sup>44</sup>. The iron nitride phases are formed by bombarding more energetic nitrogen ions on the sample surface. These impacts can dislodge iron atoms, which recombine with atmospheric nitrogen and are deposited on the sample. Saturation of the composite layer causes excess nitrogen to transfer to the inner regions of the sample, producing a diffusion layer<sup>26</sup>. In addition to SEM images, the diffusion layer can also be evidenced

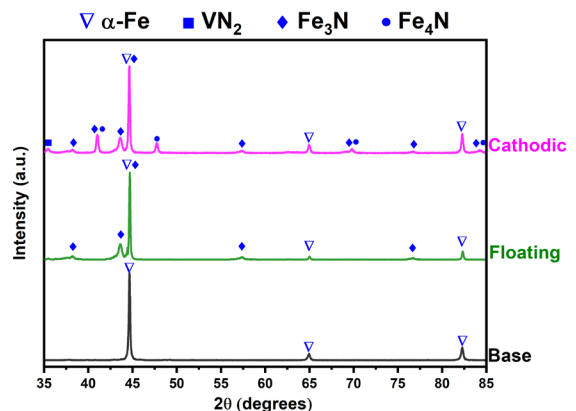


**Figure 1.** Diffraction pattern of the base material and SAE 1080 steel samples treated at cathodic and floating potentials.

by the slight shift of the  $\alpha$ -Fe phase peaks to the left. The initial microstructure of the steel, including features such as grain boundaries and defects, plays a crucial role in nitrogen diffusion and the subsequent formation of nitrides<sup>45</sup>. When the microstructure has a favorable grain distribution and an adequate density of defects, it can facilitate the absorption and diffusion of nitrogen atoms into the material<sup>46-48</sup>. Other authors report that these conditions are conducive to nitrogen atoms entering the interstices of the metallic matrix, forming both types of iron nitrides<sup>24,49,50</sup>. On the other hand, the treatment at a floating potential produced a layer with only one crystalline phase ( $\text{Fe}_3\text{N}$ ). In this case, the low occurrence of direct ion bombardment on the sample surface allows for more intense sputtering of the cage material. As a result, it was insufficient to form the  $\text{VN}_2$  phase and the diffusion zone beneath the layer, resulting in a film with the soft  $\text{Fe}_3\text{N}$  phase in its microstructure<sup>51</sup>.

It is expected that the deposited layer is sufficiently thick to suppress the diffraction peaks of the base material, and only the peaks of the sputtered material are seen in the diffractogram<sup>6,26</sup>. However, the diffraction peaks of the base material are still observed in the diffraction patterns of both cathodic and floating potential treatments, indicating that the deposited layer does not have the minimum thickness to suppress the formation of substrate diffraction peaks fully.

The coatings' average crystallite size ( $D$ ) was calculated using X-ray diffraction, with estimated values derived from the Debye-Scherrer equation<sup>52</sup>.

$$D = \frac{0.89\lambda}{\beta \cos\theta} \quad (1)$$

where  $\lambda$  is the wavelength of the radiation ( $\lambda=1.5418 \text{ \AA}$ ),  $\theta$  is the Bragg diffraction angle, and  $\beta$  corresponds to the full width at half maximum (FWHM). The estimated average crystallite size for the coatings at floating and cathodic potentials varied around 36 nm, respectively, and is reported in Table 1. In this case, it can be observed that the crystallite size is larger for the cathodic potential coating, which may be due to the higher mobility of  $\text{N}^{3-}$  ions induced in the layer formation process by the cathode potential, causing microstructural deformation in the lattice due to small changes in the  $2\theta$  values, resulting in the slight narrowing of diffraction peaks, which in turn leads to an increase in crystallite size<sup>8,9,13</sup>.

The induced lattice strain in the coatings produced at different potentials was estimated using the Williamson-Hall graphical relationship<sup>52</sup>.

$$\beta \cos\theta = \left( \frac{k\lambda}{D} \right) + 4\varepsilon \sin\theta \quad (2)$$

where  $\beta$  is the full width at half maximum,  $\lambda$  is the X-ray wavelength,  $\theta$  is the Bragg diffraction angle,  $k$  is the Debye-Scherrer constant,  $D$  is the crystallite size, and  $\varepsilon$  is the microstrain present in the crystal lattice of the coating. Figure 2 presents the Williamson-Hall plot between the y-axis ( $\beta \cos\theta$ ) and the x-axis ( $4 \sin\theta$ ), where the microstrain values were determined based on the slope of the fitted line. The diffraction angles corresponding to the  $\text{Fe}_3\text{N}$  phase peaks, joint to both treatments, are reported in Table 1. The values of the crystallite size  $D$  (WH) obtained through the Williamson-Hall relationship were close to the  $D$  (DS) values found using the Debye-Scherrer equation (Table 1).

Figure 3 shows SEM images of the morphological characteristics of the samples treated at cathodic and floating potentials. The change in polarization potential profoundly influenced the formation of the treated surfaces, resulting in distinct morphologies. A comparative examination of these surfaces provides information about the effects of vanadium cathode cage treatments at different potentials on surface characteristics. The sample subjected to cathodic potential treatment (Figure 3a) exhibits a surface characterized by clustered granular structures with relatively larger particle sizes than those formed during floating potential treatment. This phenomenon is supported by previous investigations employing cathode cage configurations under cathodic potential conditions. Morgiel et al.<sup>53</sup>, attribute the formation

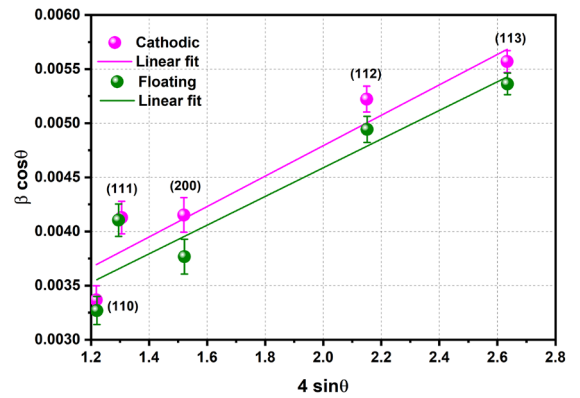
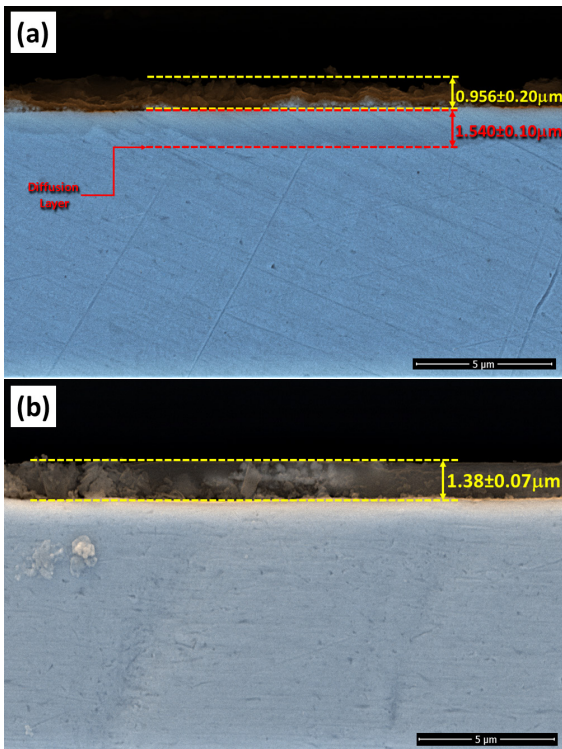


Figure 2. Williamson-Hall plots the  $\text{Fe}_3\text{N}$  phases in the nitride coatings at cathodic and floating potentials.

Table 1. Crystallite size obtained by the Debye-Scherrer equation  $D_{(DS)}$ , crystallite size  $D_{(WH)}$ , and strain  $\varepsilon_{(WH)}$  obtained by the Williamson-Hall graphical relationship.

Treatment Potential	Diffraction angle ( $2\theta$ )	Crystallite size $D_{(DS)}$ (nm)	Crystallite size $D_{(WH)}$ (nm)	Strain $\varepsilon_{(WH)}$
Cathodic	38.18	552 ± 110	782 ± 140	1.89 × 10 <sup>-3</sup>
	43.60			
	44.66			
	57.32			
	76.68			
Floating	38.20	223 ± 80	376 ± 220	1.32 × 10 <sup>-3</sup>
	43.56			
	44.70			
	57.34			
	76.70			



**Figure 3.** Surface morphology of coatings treated at cathodic (3a) and floating potentials (3b) and particle size distribution histogram of treated samples (3c cathodic potential and 3d floating potential).

of such granular structures to the interaction between ion bombardment and surface diffusion mechanisms during cathodic potential treatments. The presence of the cathode cage in the process contributes to localized variations in ion flow, which, when combined with the cathodic potential, creates irregular granular morphologies<sup>20,54,55</sup>.

On the other hand, the surface morphology resulting from the floating potential treatment (Figure 3b) exhibits a more compact and uniform structure composed of grains with consistent sizes. This type of morphology formed under floating potential conditions is frequently reported in the literature<sup>8,31,56</sup>. These observations align with Maciel de Sousa et al.<sup>57</sup>, research, which emphasizes the role of ion energy in promoting surface diffusion and the growth of uniform structures. Stable and uniform ion energy under floating potential conditions contributes to the homogeneous grain growth observed in this treatment.

Furthermore, Figures 3c and 3d provide information on grain size distributions for surfaces treated at cathodic and floating potentials. Figure 3c reveals that the coating obtained at cathodic potential exhibits an average particle size of approximately 728 nm, with size distribution ranging from 200 to 2500 nm. This variation can be attributed to deposition phenomena associated with cathodic potential treatments, as well-documented in the work of Naeem et al.<sup>25</sup>. In contrast, Figure 3d demonstrates a relatively uniform grain size profile for the floating potential treatment, with an average particle size distribution close to 350 nm. The symmetrical distribution curve reinforces the thesis of uniform grain growth in this case.

Figure 4 presents SEM images of cross-sections of the samples treated at different potentials. The thickness of the deposited layer at cathodic potential (Figure 4a) was estimated at approximately 0.95  $\mu\text{m}$ . The diffusion zone, located beneath the layer and characteristic of cathodic potential treatment, had an estimated thickness of about 1.54  $\mu\text{m}$ , demonstrating the diffusion of nitrogen ions into the steel microstructure and justifying the shift in diffraction peaks. The layer exhibits a non-uniform profile with slight thickness variations and is relatively porous. According to Naeem et al.<sup>25</sup>, the lack of uniformity in the layer occurs due to the edge effect, a common feature in plasma atmosphere processes where the sample is maintained at the cathodic potential. Considering that in this work, the plasma deposition system included the addition of the cathode cage, it is possible to justify the topographical irregularity of the layer due to the high cathodic potential generated within the cage. This potential promotes the formation of a strong electric field at the ends of the sample, directly influencing the interaction between the cage's pulverized material and the substrate surface. Thus, it may occur that some ionic species do not reach certain regions of the sample, resulting in an irregular topographical profile of the layer. The sample treated at floating potential exhibited a layer with a high degree of homogeneity and high density. The inhibition of ion bombardment and cathodic cage sputtering contributes to forming a more consolidated layer<sup>21,58</sup>. It is also noticeable that there was no formation of a diffusion zone beneath the layer, even with the appearance of iron nitride phases shown in the diffraction pattern. It is deduced that these crystallographic phases are from the nitrides present in the boundary region between the substrate surface and layer<sup>59</sup>.

Figure 5 presents the surface microhardness values of the analyzed samples. Both treated samples exhibited more excellent resistance to plastic deformation in the Vickers indentation test compared to the untreated sample. However, a more significant increase in hardness is observed in the sample subjected to cathodic treatment (550.21 HV). The presence of a composite layer followed by a non-uniform diffusion layer in the 'Cathodic' sample justifies the higher deviation in the measured Vickers hardness values<sup>56</sup>. This low uniformity results from the plasma ion bombardment on the sample, creating points of higher temperature on the material's surface and, consequently, regions of diffusion deeper than others<sup>2,55</sup>. The absence of a diffusion zone in the 'Floating' sample results in a smaller plasma-treated region than that observed in the 'Cathodic' sample (Figure 4). Therefore, this explains the lower hardness compared to the sample subjected to cathodic treatment.

The average roughness of the base sample and the plasma-treated samples reflects the quality of the topography resulting from surface modifications. The sample preparation process through grinding and polishing significantly reduced the roughness of the samples, as shown in Figure 6. The sample subjected to the floating potential treatment showed an increase in roughness due to the formation of the iron nitride composite film. The SEM image (Figure 4b) shows that this film has good uniformity compared to the modified surface of the sample subjected to cathodic potential treatment. This sample exhibited higher average roughness and a higher standard deviation of the measured values.

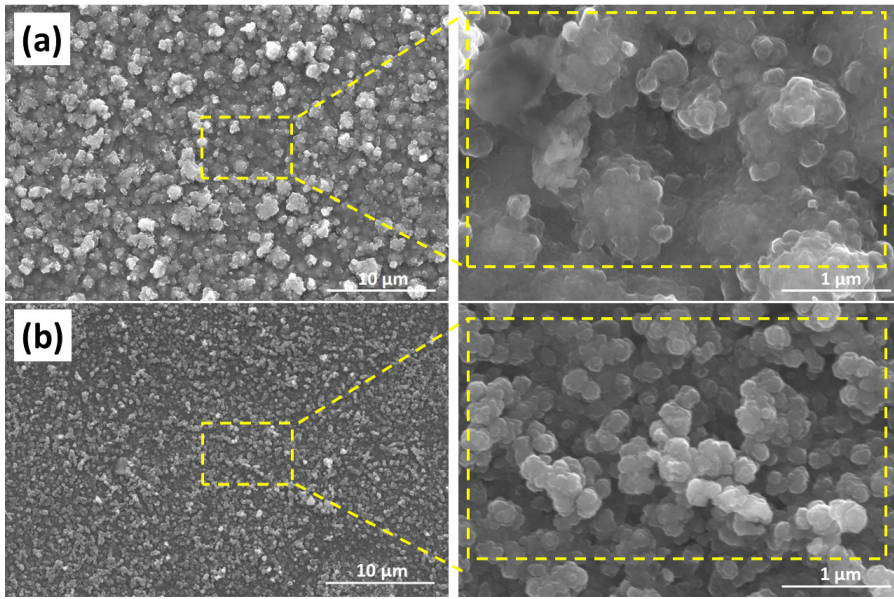


Figure 4. Cross-sectional SEM images of the nitride layers with cathode cage at cathodic potential (4a) and floating potential (4b).

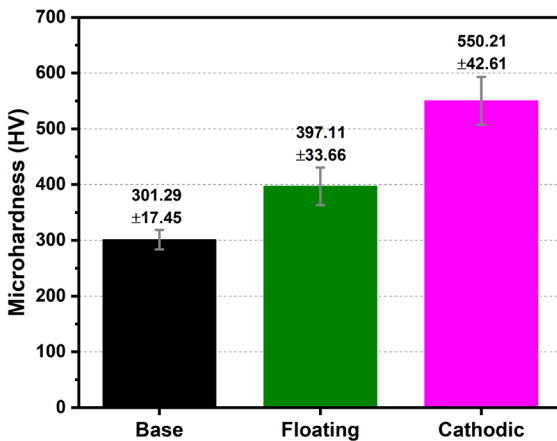


Figure 5. Microhardness of the 1080 steel samples without and with cathodic and floating potential treatment.

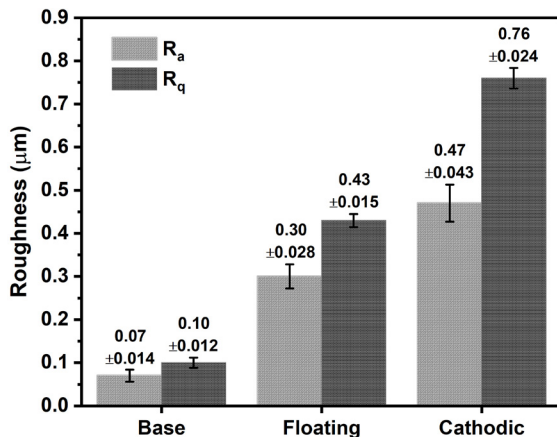


Figure 6.  $R_a$  and  $R_q$  roughness of 1080 steel samples with and without treatment.

#### 4. Conclusions

In this study, we investigated the effects of applying vanadium cage treatments at different potentials to 1080 steel, resulting in the following conclusions:

- The CCPD treatment with a vanadium cage can be used to produce composite coatings of vanadium nitride ( $\text{VN}_2$ ) with iron nitride ( $\text{Fe}_3\text{N}$  and  $\text{Fe}_4\text{N}$ ) at cathodic potential and individual iron nitride coatings at a floating polarization potential.
- The sample treated at cathodic potential consists of granular structures with irregular sizes ranging from 200 to 2500 nm. In contrast, in the floating potential treatment, the coating exhibits a high degree of uniformity, attributed to grains of uniform size that form a compact and dense structure.
- The thickness of the coatings did not vary significantly with the change in the treatments' polarization potential. However, the crystalline phase structure of each coating was directly related to the deposition kinetics of each treatment.
- The sample treated under cathodic potential showed higher resistance to plastic deformation in the Vickers indentation test due to the non-uniform diffusion layer beneath the coating. However, the sample treated under floating potential exhibited satisfactory roughness values compared to the base and cathodically treated samples, indicating a high-quality topography resulting from the surface modifications.

In CCPD deposition with a vanadium cage, it is recommended to use floating potential for iron nitride coatings and cathodic potential for coatings with specific mechanical or physical properties, such as  $\text{VN}_2$ ,  $\text{Fe}_3\text{N}$ , or  $\text{Fe}_4\text{N}$  compounds. This system is industrially viable and characterized by low treatment temperature, high process efficiency, and, consequently, short treatment time, resulting

in a good cost-benefit ratio. This study focuses exclusively on the synthesis and structural analysis of coatings generated by CCPD treatment with vanadium cages.

## 5. Acknowledgments

This study was financed in part by the Coordenação de Aperfeiçoamento de Pessoal de Nível Superior – Brasil (CAPES) – Finance Code 001.

## 6. References

- Naeem M, Díaz-Guillén JC, Khalid A, Guzmán-Flores I, Muñoz-Arroyo R, Iqbal J, et al. Improved wear resistance of AISI-1045 steel by hybrid treatment of plasma nitriding and post-oxidation. *Tribol Int.* 2022;175:107869.
- Schibicheski Kurelo BCE, Souza GB, Serbena FC, de Oliveira WR, Marino CEB, Taminato LA. Performance of nitrogen ion-implanted supermartensitic stainless steel in chlorine- and hydrogen-rich environments. *Surf Coat Tech.* 2018;351:29-41.
- Niu R, Li J, Wang Y, Chen J, Xue Q. Structure and high temperature tribological behavior of TiAlN/nitride duplex treated coatings on Ti6Al4V. *Surf Coat Tech.* 2017;309:232-41.
- Navarro-Devia JH, Amaya C, Caicedo JC, Martínez JH, Aperador W. Hafnium and vanadium nitride multilayer coatings [HfN/VN]<sub>n</sub> deposited onto HSS cutting tools for dry turning of a low carbon steel: a tribological compatibility case study. *Int J Adv Manuf Technol.* 2019;101(5):2065-81.
- Kim H-B, Ngo DT, Verma R, Singhababu YN, Kim D, Le HTT, et al. Vanadium nitride and carbon nanofiber composite membrane as an interlayer for extended life cycle lithium-sulphur batteries. *Ceram Int.* 2021;47(15):21476-89.
- Tripathy PK. On the thermal decomposition of vanadium nitride. *J Mater Chem.* 2001;11(5):1514-8.
- Han Y, Zhang S, Bai R, Zhou H, Su Z, Wu J, et al. Effect of nano-vanadium nitride on microstructure and properties of sintered Fe-Cu-based diamond composites. *Int J Refract Hard Met.* 2020;91:105256.
- Qiu W, Xie W, Li Q-F, Huang W-Y, Zhou L-B, Chen W, et al. Effect of vanadium nitride (VN) particles on microstructure and mechanical properties of extruded AZ31 Mg alloy. *Acta Metall Sin.* 2023;36(2):237.
- Venkateshalu S, Cherusseri J, Karnan M, Kumar KS, Kollu P, Sathish M, et al. New method for the synthesis of 2D Vanadium Nitride (MXene) and its application as a supercapacitor electrode. *ACS Omega.* 2020;5(29):17983-92.
- Rizzo A, Goel S, Luisa Grilli M, Iglesias R, Jaworska L, Lapkovskis V, et al. The critical raw materials in cutting tools for machining applications: a review. *Materials.* 2020;13(6):1377.
- Yin Q, Xu P, Chen X, Liu L, Liu B, Yang L, et al. Mechanism and experimental study on preparation of high-quality vanadium nitride by one-step vacuum carbothermal reduction nitridation method. *Vacuum.* 2023;208:111672.
- Ma C-H, Huang J-H, Chen H. A study of preferred orientation of vanadium nitride and zirconium nitride coatings on silicon prepared by ion beam assisted deposition. *Surf Coat Tech.* 2000;133-134:289-94.
- Caicedo JC, Zambrano G, Aperador W, Escobar-Alarcon L, Camps E. Mechanical and electrochemical characterization of vanadium nitride (VN) thin films. *Appl Surf Sci.* 2011;258(1):312-20.
- Aissani L, Fellah M, Chadli AH, Samad MA, Cheriet A, Salhi F, et al. Investigating the effect of nitrogen on the structural and tribo-mechanical behavior of vanadium nitride thin films deposited using R.F. magnetron sputtering. *J Mater Sci.* 2021;56(30):17319-36.
- Van Meter KE, Chowdhury MI, Sowa MJ, Kozen AC, Grejtak T, Babuska TF, et al. Effects of deposition temperature on the wear behavior and material properties of plasma enhanced atomic layer deposition (PEALD) titanium vanadium nitride thin films. *Wear.* 2023;523:204731.
- Di L, Zhang J, Zhang X, Wang H, Li H, Li Y, et al. Cold plasma treatment of catalytic materials: a review. *J Phys D Appl Phys.* 2021;54(33):333001.
- Abreu LHP, Naeem M, Borges WFA, Monção RM, Sousa RRM, Abrar M, et al. Synthesis of TiN and TiO<sub>2</sub> thin films by cathodic cage plasma deposition: a brief review. *J Braz Soc Mech Sci Eng.* 2020;42(9):496.
- Liu Y, Wu Q, Liu L, Manasa P, Kang L, Ran F. Vanadium nitride for aqueous supercapacitors: a topic review. *J Mater Chem A Mater Energy Sustain.* 2020;8(17):8218-33.
- Liu R, Yang L, Wang W, Zhao E, Wang B, Zhang X, et al. Surface redox pseudocapacitance-based vanadium nitride nanoparticles toward a long-cycling sodium-ion battery. *Mater Today Energy.* 2023;34:101300.
- Deus GP, Monção RM, Almeida LS, Rossino LS, Costa THC, Libório MS, et al. Surface analysis of AISI D2 steel treated by plasma nitriding and niobium and vanadium nitride films by cathodic cage plasma deposition. *Braz J Phys.* 2022;53(1):10.
- Naeem M, Qadeer M, Mujahid Z, Rehman NU, Díaz-Guillén JC, Sousa RRM, et al. Time-resolved plasma diagnostics of cathodic cage plasma nitriding system with variable pulsed duty cycle and surface modification of plain carbon steel. *Surf Coat Tech.* 2023;464:129542.
- Sousa RRM, Araújo FO, Ribeiro KJB, Mendes MWD, Costa JAP, Alves C Jr. Cathodic cage nitriding of samples with different dimensions. *Mater Sci Eng A.* 2007;465(1):223-7.
- Li CX, Bell T, Dong H. A study of active screen plasma nitriding. *Surf Eng.* 2002;18(3):174-81.
- Skobir Balantić DA, Donik Č, Podgornik B, Kocijan A, Godec M. Improving the surface properties of additive-manufactured Inconel 625 by plasma nitriding. *Surf Coat Tech.* 2023;452:129130.
- Naeem M, Fortaleza VC, Serra PLC, Lima CL, Costa THC, Sousa RRM, et al. Synthesis of molybdenum oxide on AISI-316 steel using cathodic cage plasma deposition at cathodic and floating potential. *Surf Coat Tech.* 2021;406:126650.
- Silva LGL, Naeem M, Costa THC, Libório MS, Bandeira RM, Ferreira NS, et al. Wear and corrosion of UNS S32750 steel subjected to nitriding and cathodic cage deposition. *J Mater Eng Perform.* 2023;32(20):9011-8.
- Naeem M, Awan S, Shafiq M, Raza HA, Iqbal J, Díaz-Guillén JC, et al. Wear and corrosion studies of duplex surface-treated AISI-304 steel by a combination of cathodic cage plasma nitriding and PVD-TiN coating. *Ceram Int.* 2022;48(15):21473-82.
- Alves C Jr, Araújo FO, Ribeiro KJB, Costa JAP, Sousa RRM, Sousa RS. Use of cathodic cage in plasma nitriding. *Surf Coat Tech.* 2006;201(6):2450-4. <http://dx.doi.org/10.1016/j.surfcoat.2006.04.014>.
- Dong Y, Li X, Tian L, Bell T, Sammons RL, Dong H. Towards long-lasting antibacterial stainless steel surfaces by combining double glow plasma silvering with active screen plasma nitriding. *Acta Biomater.* 2011;7(1):447-57.
- Fernandes FM, Rocha EA Fo, Souza IA, Nascimento IO, Sousa RRM, Almeida EO, et al. Deposition of fine copper film on samples placed internally and externally to the cathodic cage. *Int J Mater Res.* 2019;110(3):275-80.
- Liu J, Wang X, Hu Y, Luo L, Jiang C, Liu F, et al. Effect of hydrogen on microstructure and mechanical properties of plasma-nitrided pure titanium by cathodic cage plasma nitriding. *Surf Coat Tech.* 2023;456:129231.
- Morell-Pacheco A, Kim H, Wang T, Shiao C-H, Balerio R, Gabriel A, et al. Ni coating on 316L stainless steel using cage plasma treatment: feasibility and swelling studies. *J Nucl Mater.* 2020;540:152385.

33. Toshioka N, Nishimoto A. Surface-modified layer formed by plasma nitriding using chromium screen. *Mater Trans.* 2020;61(6):1115-21.
34. Kovács D, Dobránszky J, Fodor T, Takáts V, Bonyár A. Investigation of the ASPN process of low alloy steel by using Ni or Cr coated active screens. *Surf Coat Tech.* 2020;394:125638.
35. Macedo FRC, Monção RM, Queiroz JCA, Libório MS, Costa JAP, Rossino LS, et al. Study of surface modification of niobium caused by nitriding and cathodic cage deposition. *Mater Res.* 2023;26:e20220613.
36. Medeiros MV Fo, Silva LP, Libório MS, Queiroz JCA, Coan KS, Rossino LS, et al. Film deposition by duplex treatment with hastelloy cage on AISI 6160 Steel. *Mater Res.* 2023;26:e20220625.
37. Shafique A, Naveed MA, Ijaz S, Zubair M, Mehmood MQ, Massoud Y. Highly efficient Vanadium Nitride based metasurface absorber/emitter for solar-thermophotovoltaic system. *Mater Today Commun.* 2023;34:105416.
38. Huang T, Mao S, Zhou G, Wen Z, Huang X, Ci S, et al. Hydrothermal synthesis of vanadium nitride and modulation of its catalytic performance for oxygen reduction reaction. *Nanoscale.* 2014;6(16):9608.
39. Escobar CA, Caicedo JC, Aperador W. Corrosion resistant surface for vanadium nitride and hafnium nitride layers as function of grain size. *J Phys Chem Solids.* 2014;75(1):23-30.
40. Barbosa MGC, Viana BC, Santos FEP, Fernandes F, Feitor MC, Costa THC, et al. Surface modification of tool steel by cathodic cage TiN deposition. *Surf Eng.* 2021;37(3):334-42.
41. Sousa RRM, Sato PS, Viana BC, Alves C Jr, Nishimoto A, Nascente PAP. Cathodic cage plasma deposition of TiN and TiO<sub>2</sub> thin films on silicon substrates. *J Vac Sci Technol A.* 2015;33(4):041502.
42. Sousa FA, Costa JAP, Sousa RRM, Barbosa JCP, Araújo FO. Internal coating of pipes using the cathodic cage plasma nitriding technique. *Surf Interfaces.* 2020;21:100691.
43. Nishimoto A, Bell TE, Bell T. Feasibility study of active screen plasma nitriding of titanium alloy. *Surf Eng.* 2010;26(1-2):74-9.
44. Naeem M, Shafiq M, Zaka-ul-Islam M, Nawaz N, Díaz-Guillén JC, Zakaullah M. Effect of cathodic cage size on plasma nitriding of AISI 304 steel. *Mater Lett.* 2016;181:78-81.
45. Kusmanov SA, Smirnov AA, Belkin PN. Features of nitroquenching of medium-carbon steel during anodic electrolyte-plasma processing. *Prot Met Phys Chem Surf.* 2016;52(1):133-9.
46. Eresko SP, Ivanov YF, Lopatin IV, Klopotov AA, Nikonenko AV. Structure of the surface layer of high-chrome steel nitridated in the elion regime in the plasma of a suspended arc discharge with a heated cathode. *Siberian Aerospace Journal.* 2023;24(1):168-76.
47. Belkin PN, Kusmanov SA. Plasma electrolytic nitriding of steels. *J Surf Invest X-ray, Synchrotron Neutron Tech.* 2017;11(4):767-89.
48. He F, Zhao J, Hu Q, Liu Y, Huang Q, You Z, et al. Gas-based reduction and nitridation for synthesis of vanadium nitride: kinetics and mechanism. *Powder Technol.* 2023;427:118757.
49. Jo M-G, Madakashira PP, Suh J-Y, Han HN. Effect of oxygen and nitrogen on microstructure and mechanical properties of vanadium. *Mater Sci Eng A.* 2016;675:92-8.
50. Drouet M, Le Bourhis E. Low temperature nitriding of metal alloys for surface mechanical performance. *Materials.* 2023;16(13):4704.
51. Macedo FRC, Sousa RRM, Nogueira JW Jr, Luz-Lima C, Libório MS, Lobo AO, et al. Tribological behavior of SINTER30 steel subjected to duplex treatment. *Steel Res Int.* 2023;94(6):2200760.
52. Mustapha S, Ndamitso MM, Abdulkareem AS, Tijani JO, Shuaib DT, Mohammed AK, et al. Comparative study of crystallite size using Williamson-Hall and Debye-Scherrer plots for ZnO nanoparticles. *Adv. Nat. Sci: Nanosci. Nanotechnol.* 2019;10(4):045013.
53. Morgiel J, Maj Ł, Szymkiewicz K, Pomorska M, Ozga P, Tobała D, et al. Surface roughening of Ti-6Al-7Nb alloy plasma nitrided at cathode potential. *Appl Surf Sci.* 2022;574:151639.
54. Naeem M, Torres AVR, Serra PLC, Monção RM, Antônio CA Jr, Rossino LS, et al. Combined plasma treatment of AISI-1045 steel by hastelloy deposition and plasma nitriding. *J Build Eng.* 2022;47:103882.
55. Sousa RRM, Moura YJL, Sousa PAO, Medeiros JQ No, Costa THC, Alves C Jr. Nitriding of AISI 1020 steel: comparison between conventional nitriding and nitriding with cathodic cage. *Mater Res.* 2014;17(3):708-13.
56. Naeem M, Zaka-ul-Islam M, Shafiq M, Bashir MI, Díaz-Guillén JC, Zakaullah M. Influence of cathodic cage diameter on mechanical properties of plasma nitrided AISI 304 steel. *Surf Coat Tech.* 2017;309:738-48.
57. Maciel de Sousa E, Bruno de Vasconcelos Leitão A, Carvalho Serra PL, Borges JO, Vega ML, Moura JVB, et al. Surface modification of AISI 316 steel by  $\alpha$ -MoO<sub>3</sub> thin films grown using cathodic cage plasma deposition. *Physica B.* 2023;648:414410.
58. Lima LFF, Libório MS, Medeiros JF No, Coan KS, Rossino LS, Sousa RRM, et al. Plasma deposition of solid lubricant coating using AISI1020 steel cathode cylinders technique. *Mater Res.* 2023;26:e20220623.
59. Sousa RRM, Araújo FO, Costa JAP, Dumelow T, Oliveira RS, Alves C. Nitriding in cathodic cage of stainless steel AISI 316: influence of sample position. *Vacuum.* 2009;83(11):1402-5.